ChemComm

Accepted Manuscript

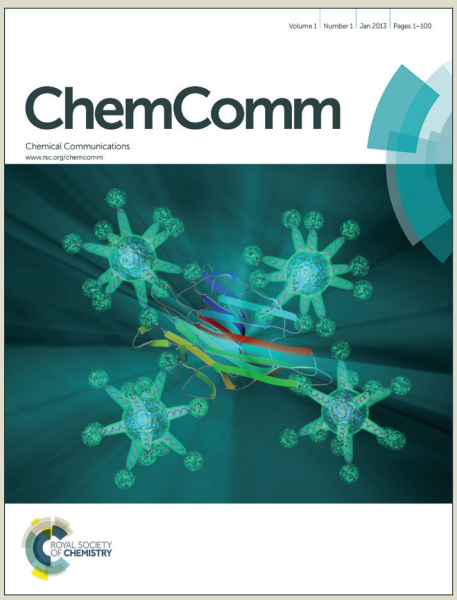

ROYAL SOCIETY OF CHEMISTRY

www.rsc.org/chemcomm

Cite this: DOI: 10.1039/c0xx00000x

www.rsc.org/xxxxxx

ARTICLE TYPE

Novel mesoporous carbon@silicon-silica nanostructure for high-performance Li-ion battery anode

Qianjun He,*[a,b] Chaohe Xu,[a] Jianqiang Luo,[a] Wei Wu,[a] Jianlin Shi*[a]

Received (in XXX, XXX) Xth XXXXXXXXX 20XX, Accepted Xth XXXXXXXXX 20XX

DOI: 10.1039/b000000x

A novel hierarchical nanostructure with graphite-like carbon and small Si nanocrystals respectively encapsulated in the mesopores and embedded in the silica framework of mesoporous silica nanoparticles has been facilely constructed and used as anode for Li-ion battery, which exhibits high specific storage capacity and extraordinarily high cycling stability.

With ever-increasing energy demands in next-generation portable electronic devices, recent research and development have been focused on new electrode materials with high energy density and superior cycling stability for the next generation of Li-ion batteries (LIBs). There has therefore been great interest in developing new anode materials with relative high theoretical specific capacities, such as tin oxides, cobalt oxides, iron oxides, manganese oxides, Ge, Sn, Sb, *etc*.[1] However, the main disadvantage of these anodes is large volume variation during the lithium insertion/extraction processes. Such a volume variation results in pulverization of electrode and loss of electrical contact with current collectors, which severely degrades their cycling stability and leads to their capacity loss. Comparatively, silicon has the highest theoretical capacity (4212 mA h g^{-1} for $Li_{4.4}Si$) reported so far,[2a] however unfortunately, the poor cycling performance resulted inevitably from the severe volume effect and pulverization has become one of most critical adverse factors affecting its applications.[2b] Recent efforts have indicated that this problem is resolvable by decreasing the particle size of silicon,[3] dispersing silicon nanoparticles into an inactive/active matrix,[4] or coating with conductive polymers[5] or/and carbon[6,7] or/and silica,[7,8] *etc*. Particularly, silicon@silica/carbon nanocomposites as anode materials can integrate advantages of carbon (long cycle life) and silicon (high specific capacity) to remarkably improve overall electrochemical performances of LIBs, especially the cycling stability.[7b]

However, silicon has a low electrical conductivity intrinsically, therefore the silicon-based anode materials are desired to be made into porous nanocomposites with graphitic/graphite-like carbon to overcome this disadvantage because graphitic/graphite-like carbon has remarkably higher electrical conductivity[6,7] while a porous structure can provide: (i) short diffusion path of lithium ions within the nano-sized pore walls, (ii) easy electrolyte penetration through the pores, and (iii) highly available charge storage sites owing to high surface area.[5,6a,9] In this way, the integration of silicon-silica-carbon nanocomposites into a porous structure as anode is highly promising to improve the overall electrochemical performances of silicon-based LIBs.

Here, we employ a bottom-up self-assembly route to synthesize a kind of oxygen-deficient mesoporous silica nanoparticles (MSNs), and then develop an *in situ* carbonization/crystallization route to facilely construct a novel type of hierarchical nanostructure with graphitized carbon encapsulated in the mesopores and Si nanocrystals embedded within the mesoporous silica framework of MSNs (mesoporous C@Si-SiO_2 nanostructures, abbreviated to 'MCSSNs'), as shown in Scheme 1. It is worth noting that the *in situ* encapsulated carbon is partially graphitized and has a close contact with the mesoporous silica framework, greatly favoring the electron transfer. Furthermore, the mesoporous structure of MCSSNs can provide a high surface area in favor of transfer and reaction of lithium ions, while the Si@SiO_2 mosaic structure of mesoporous framework can prevent Si nanocrystals from pulverization and thus endow the MCSSNs-based LIBs with superior cycling performance and high reversible capacity.

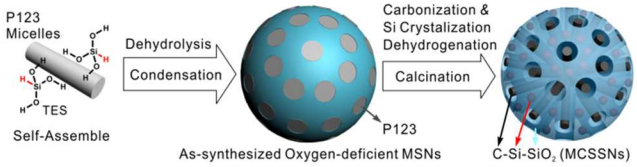

Scheme 1 Schematic Illustration for the Synthesis of MCSSNs.

As illustrated by Scheme 1, the oxygen-deficient MSNs were synthesized by using Pluronic P123 as a structure-directing agent (SDA) and triethoxysilane (TES) as a special silicon source by a bottom-up self-assembly route, as reported previously by us.[10] Our previous researches indicated that the post-calcination at 600 °C can dehydrogenize O_3Si–H terminal groups to create copious oxygen vacancies capable of generating luminescence,[11] and therefore the synthesized luminescent mesoporous silica was used for drug delivery and synchronous imaging.[10] As for applications for LIB anode, this work proposed to crystallize Si nanoparticles in the oxygen-deficient mesoporous silica framework for the first time, and thus the calcination temperature is necessarily as high as 900 °C. However, MSNs without P123 would be subject to loss of their porous structures at such a high calcination temperature.[10] In this work, we fortunately discover that the P123 micelles reserved within the mesopores of MSNs can be *in situ* carbonized at 900 °C under inert atmosphere, and support the

mesostructure from collapse, and meanwhile Si nanocrystals could also be generated *in situ* within the mesoporous framework during high temperature calcination (900 °C), as shown in Scheme 1. Compared with our previous report about the oxygen-deficient luminescent MSNs for bio-applications, the present MCSSNs is synthesized by a smarter and novel *in situ* carbonization/crystallization route, and have a remarkably different nanostructure with Si nanocrystals embedded within the mesoporous silica framework and graphitized carbon encapsulated in the mesopores in favor of applications as LIB anode materials.

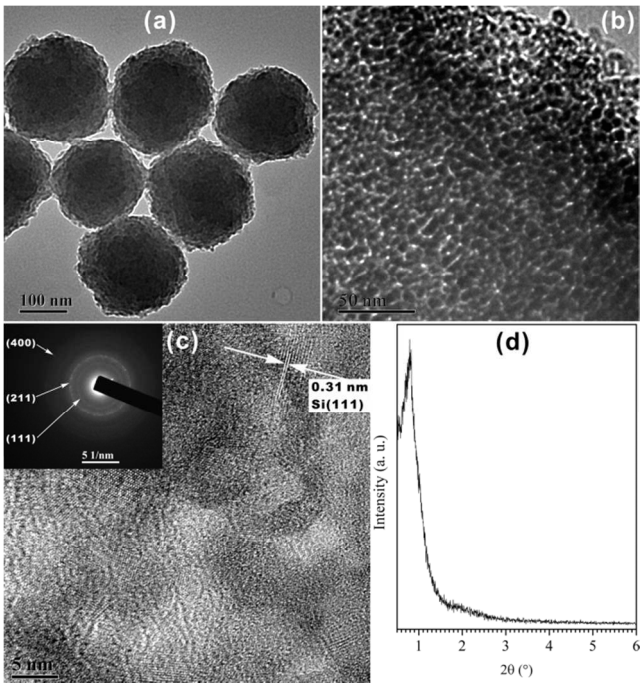

Fig. 1 TEM images (a−c) and SA-XRD pattern (d) of MCSSNs. Figure c is a HR-TEM image of MCSSNs, where the inset is the corresponding SAED pattern.

The morphology and mesostructure of MCSSNs were observed through TEM imaging (Fig. 1a−c). It could be found that MCSSNs possess uniform particle size of about 200 nm, spherical morphology (Fig. 1a) and well-defined mesoporous structure (Fig. 1b) even though the post-calcination temperature was as high as 900 °C. Moreover, the sharp small-angle X-ray diffraction (SA-XRD) peaks at 0.6–0.8° (Fig. 1d and Supplementary Fig. S1a) also indicate that both the as-synthesized MSNs and MCSSNs possess partially ordered mesoporous structures.[12] If P123 was removed by solvent extraction before calcination, the mesoporous structure of MSNs would be destroyed after post-calcination above 600 °C, as indicated previously by us.[10] Therefore it is thought that the *in situ* carbonization of P123 micelles within the mesopores of MSNs is of great benefit to support the mesoporous structure. Nitrogen adsorption–desorption measurement also indicates that MCSSNs have a relatively high porosity with specific surface area of 85 m^2/g, pore volume of 0.2 m^3/g and pore diameter of 3.8 nm (Supplementary Fig. S2), which is expected to favor an evener lithium concentration distribution across the electrode material and thus more uniform volume changes during lithium insertion/extraction processes, avoiding the electrode pulverization.[3c,9] From SEM images, it could also be found that both the as-synthesized MSNs (Supplementary Fig. S3a) and MCSSNs (Supplementary Fig. S3b) have uniform particle size and spherical shape, further indicating little effect of high temperature calcination on the morphology of MCSSNs in the present experimental conditions.

Furthermore, a hierarchical nanostructure with Si nanocrystals of about 3 nm embedded within the mesoporous silica framework is observable under the high-resolution TEM (HR-TEM) imaging, as suggested by the clear (111) lattice fringes of the diamond cubic Si phase with a (111) interplanar spacing of 0.31 nm and the corresponding selected area electron diffraction (SAED) pattern (inset of Fig. 1c).[7b,9d] Moreover, the Si crystallization could also been confirmed by two broad diffraction peaks of MCSSNs at 28.9° and 47.5° in wide-angle XRD patterns (Supplementary Fig. S1b), which can be indexed as (111) and (220) planes of cubic Si (JCPDF card No. 27-1402), respectively. In addition, both the as-synthesized MSNs and MCSSNs exhibit a wide diffraction peak at 22.5° (Supplementary Fig. S1b), which should be assigned to amorphous silica framework. Furthermore, MCSSNs still exhibited a well-defined diffraction peak at 26.5° (Supplementary Fig. S1b), which can be indexed as the (002) plane of graphite (JCPDF card No. 41-1487).

To investigate the P123 carbonization within MSNs, the Raman and FTIR spectra of the as-synthesized MSNs sample and the post-calcined MCSSNs sample were collected (Supplementary Fig. S4 and Fig. S5). It could be found that the as-synthesized MSNs sample exhibits several characteristic adsorption bands of P123 at 2980–2850 cm^{-1} and 1460–1370 cm^{-1}, ascribing to CH_3/CH_2 stretching and bending vibrations, respectively. However, these characteristic adsorption bands of P123 are invisible after post-calcination at 900 °C under nitrogen blowing protection, as shown by the black MCSSNs sample (Supplementary Fig. S4). This suggests that P123 encapsulated within MSNs has been carbonized. Furthermore from the Raman spectrum of carbon sorted from MCSSNs (Supplementary Fig. S5), two characteristic Raman bands of graphite-like carbon at 1560 cm^{-1} (G band) and 1300 cm^{-1} (D band) can be distinctly identified,[9d] further indicating the partial graphitization of P123 within MCSSNs in accordance with the above-mentioned wide-angle XRD results. The carbon content of MCSSNs was determined to be 22.1 wt.% by elemental analysis. The graphite-like carbon *in situ* encapsulated within the mesopores of MCSSNs will favour the electrochemical performances of MCSSNs. The P123 carbonization and the Si crystallization within MCSSNs were also verified further by TG/DTA/DTG thermal analysis (Supplementary Fig. S6) and FTIR measurement (Supplementary Fig. S4).

The lithium-storage properties of MCSSNs nanocomposite electrodes were investigated. From the galvanostatic charge−discharge curves (Fig. 2a), MCSSNs nanocomposite electrodes exhibit high charging and discharging capacities of 2022 and 888 mA h g^{-1}, 1350 and 583 mA h g^{-1}, 958 and 415 mA h g^{-1} at current densities of 100, 150 and 500 mA g^{-1}, respectively, in the first cycles. Though there are large capacity losses (irreversibility) in the first charging−discharging process,

the Coulombic efficiencies are generally higher than 99% at various current densities after the first cycle, as indicated by Supplementary Fig. S7. Generally, the capacitive irreversibility of silicon-based electrodes in LIBs in the first initial cycle is a prevailing phenomenon, and the initial irreversible capacity loss could mainly arise from the formation of a solid electrolyte interphase on the surface of the active particles and/or the irreversible lithium insertion.[9d] Even so, the reversible capacities of MCSSNs nanocomposite electrodes are still as high as about 920, 600 and 420 mA h g^{-1} at current densities of 100, 150 and 500 mA g^{-1}, respectively (Supplementary Fig. S7). The most important thing is that the cycling performance investigation indicated that MCSSNs nanocomposite electrodes exhibited excellent cyclability (up to 500 cycles in Supplementary Fig. S8), and the specific capacities were well retained and even increased slightly with the increase of cycle time at different current densities (Supplementary Fig. S7 and Fig. 2b). By comparison, bare Si particles would deliver the irreversible capacities with continuing and rapid reduction after cycling in spite of considerably high first charging−discharging capacities, which was mainly resulted from the pulverization of silicon particles and the microstructural damage during lithium insertion/extraction processes.[13] Therefore, the outstanding cycling performance of MCSSNs nanocomposite electrodes could be attributed to the stable embedding structure of Si nanocrystals within the mesoporous silica framework forming a three-dimensional mosaic-like architecture, and both the silicon nanocrystals and the whole spherical particles retained their integrity without significant volume change and pulverization during calcination at 900 °C and after 100 charge−discharge cycles, as indicated by TEM images in Fig. 1c and Supplementary Fig. S9, respectively. Moreover compared with various carbon anode materials (graphite, graphene, carbon nanotubes, fullerenes),[14] MCSSNs nanocomposite electrodes have remarkably higher specific storage capacity and comparable or even better cycling stability. In addition, the gradual and slight increase in the specific capacity of MCSSNs, which is a common phenomenon for many nanostructured electrodes,[5c,15] could result from the gradual activation of MCSSNs electrodes and the enhancement of the electrical conductivity of electrodes in large numbers of repeated charging−discharging processes as discussed below.

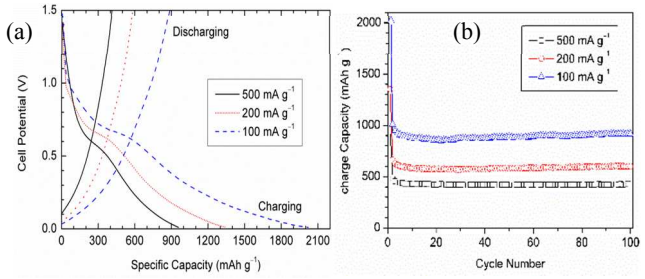

Fig. 2 Galvanostatic charge−discharge curves (a) and cycling performances (b) of MCSSNs electrodes at current densities of 100, 150 and 500 mA g^{-1}.

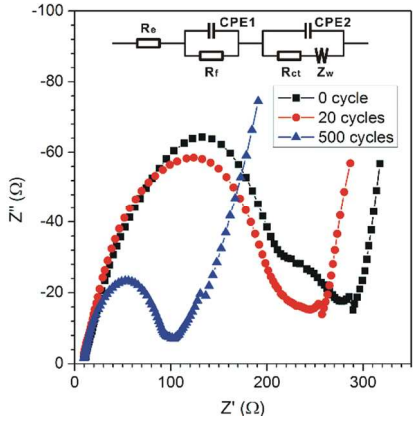

Fig. 3 Electrochemical impedance spectra of MCSSNs electrodes before and after cycling obtained by applying a sine wave with amplitude of 5.0 mV over the frequency range from 100 kHz to 10 mHz.

Table 1 Electrochemical impedance fitted parameters of MCSSNs before and after cycling with an equivalent circuit model shown in Fig. 3.

Cycle Number	R_e (Ω)	R_f (Ω)	R_{ct} (Ω)
0	9.1	200.4	151.3
20	6.4	186.1	140.3
500	8.5	85.5	89.6

Furthermore to get insight into the electrochemical properties of the MCSSNs nanocomposite electrode, the electrochemical impedance spectra (EIS) before and after cycling were measured (Fig. 3), and the EIS parameters were obtained by fitting experimental data with an equivalent circuit model[14a,14b,16] shown in the inset of Fig. 3 (Table 1). Therein, R_e represents the internal resistance of the tested battery; R_f and CPE1 are associated with the constant resistance and constant phase element of the solid-electrolyte interphase (SEI) film, corresponding to the semicircle in the high-frequency region; R_{ct} and CPE2 are associated with the charge-transfer resistance and constant phase element of the electrode/electrolyte interface, corresponding to the medium-frequency semicircle; Z_w is associated with the Warburg impedance, corresponding to the lithium-diffusion process. From Fig. 3, the diameter of the high-frequency semicircle clearly becomes smaller after cycling, indicating that the contact impedance (R_f) becomes lower; the diameter of the medium-frequency semicircle remarkably becomes smaller after cycling, revealing that the charge-transfer impedance (R_{ct}) becomes lower; the low-frequency inclined line indicates that the diffusion of Li ions is easy, probably owing to the special nanostructure of MCSSNs (C@Si-SiO_2) with graphite-like carbon and small Si nanocrystals respectively encapsulated in the mesopores and embedded in the silica framework as mentioned above. From the fitted results in Table 1, it can be further found that the SEI resistance (R_f) and charge-transfer resistance (R_{ct}) of the MCSSNs nanocomposite electrode are 200.4 Ω and 151.3 Ω before cycling, and remarkably decrease with the increase of cycling time down to 85.5 Ω and 89.6 Ω after 500 cycles. This indicates that the contact between electrode and electrolyte as well as the electrical conductivity of the overall electrode can be

improved during cycling. It is thought to be derived from the gradual immersion of electrolyte into the mesoporous structure of the MCSSNs and the conductivity increase of Si nanoparticles within the MCSSNs after lithium-ion doping associated with electrochemical charging. The significant improvement of the electrical conductivity of the overall MCSSNs electrode might be a reason for the gradual and slight increase in the specific capacity of MCSSNs during cycling as mentioned above.[5b]

In conclusion, a novel kind of hierarchical nanostructure with graphite-like carbon encapsulated in the mesopores and with Si nanocrystals of about 3 nm embedded within the silica framework of MCSSNs, exhibiting relatively high porosity, uniform particle size (200 nm) and well-defined spherical morphology, has been successfully constructed by a facile bottom-up self-assembly strategy followed by an *in situ* carbonization/crystallization approach. The reservation of P123 in the mesopores for *in situ* carbonization, the utilization of TES as the especial Si source for the generation of copious oxygen vacancies and the post-calcination at 900 °C for *in situ* Si crystallization within the silica framework are three important factors to construct MCSSNs with hierarchical nanostructure. MCSSNs as a Li-battery anode material exhibited high reversible specific storage capacity (920 mA h g^{-1} at current density of 100 mA g^{-1}) and long cycling life (beyond 500 cycles with Coulombic efficiencies of higher than 99%), and would therefore have potential applications in high-performance LIBs.

We acknowledge the financial support from the National Nature Science Foundation of China (Grant Nos. 51102259 and 51132009) and the Marie Curie International Incoming Fellowship within the 7th European Community Framework Programme (Grant No. PIIF-GA-2011–299636).

Notes and references

[a] *State Key Laboratory of High Performance Ceramics and Superfine Microstructure, Shanghai Institute of Ceramics, Chinese Academy of Sciences, 1295 Ding-Xi Rd. Shanghai 200050, P. R. China. Fax: 86 21 52413122; Tel: 86 21 52412714; E-mail: nanoflower@126.com*

[b] *School of Chemistry, University of Leeds, Woodhouse Lane, Leeds LS2 9JT, UK*

† Electronic Supplementary Information (ESI) available: Experimental details for the synthesis, galvanostatic discharge–charge curves, SEM and TEM images, XRD patterns, nitrogen adsorption–desorption data, Raman and FTIR spectra, and TG/DTA/DTG curves. See DOI: 10.1039/b000000x/

1 (a) J. Liu, S. Z. Qiao, J. S. Chen, X. W. Lou, X. R. Xing and G. Q. Lu, *Chem. Commun*., 2011, **47**, 12578; (b) X. Xin, X. F. Zhou, F. Wang, X. Y. Yao, X. X. Xu, Y. M. Zhu and Z. P. Liu, *J. Mater. Chem*., 2012, **22**, 7724; (c) S. Ding, J. S. Chen, G. Qi, X. Duan, Z. Wang, E. P. Giannelis, L. A. Archer and X. W. Lou, *J. Am. Chem. Soc*., 2011, **133**, 21; (d) Z. Y. Wang, Z. C. Wang, S. Madhavi and X. W. Lou, *J. Mater. Chem*., 2012, **22**, 2526; (e) R. Z. Hu, H. Liu, M. Q. Zeng, J. W. Liu and M. Zhu, *J. Mater. Chem*., 2012, **22**, 9539; (f) M. T. Sougrati, J. Fullenwarth, A. Debenedetti, B. Fraisse, J. C. Jumas and L. Monconduit, *J. Mater. Chem*., 2011, **21**, 10069.

2 (a) B. A. Boukamp, G. C. Lesh and R. A. Huggins, *J. Electrochem. Soc*., 1981, **128**, 725; (b) U. Kasavajjula, C. Wang and A. J. Appleby, *J. Power Sources*, 2007, **163**, 1003.

3 (a) C. K. Chan, H. Peng, G. Liu, K. McIlwrath, X. F. Zhang, R. A. Huggins and Y. Cui, *Nature Nanotechnol*., 2008, **3**, 31; (b) M. Holzapfel, H. Buqa, L. J. Hardwick, M. Hahn, A. Würsig, W. Scheifele, P. Novák, R. Kötz, C. Veit and F.-M. Petrat, *Electrochim. Acta*, 2006, **52**, 973; (c) J. Graetz, C. C. Ahn, R. Yazami and B. Fultz, *Electrochem. Solid-State Lett*. 2003, **6**, A194.

4 (a) I.-S. Kim, P. N. Kumta and G. E. Blomgren, *Electrochem. Solid-State Lett*., 2000, **3**, 493; (b) I.-S. Kim, G. E. Blomgren and P. N. Kumta, *Electrochem. Solid-State Lett*., 2003, **6**, A157; (c) Z. P. Guo, Z. W. Zhao, H. K. Liu and S. X. Dou, *J. Power Sources*, 2005, **146**, 190.

5 (a) G. Yu, X. Xie, L. Pan, Z. Bao and Y. Cui, *Nano Energy*, 2013, **2**, 213; (b) H. Wu, G. Yu, L. Pan, N. Liu, M. T. McDowell, Z. Bao and Y. Cui, *Nature Commun*., 2013, **4**, 1943; (c) B. Liu, P. Soares, C. Checkles, Y. Zhao, G. Yu, *Nano Lett*., 2013, **13** 3414.

6 (a) A. Magasinski, P. Dixon, B. Hertzberg, A. Kvit, J. Ayala and G. Yushin, *Nature Mater*., 2010, **9**, 353; (b) J. Saint, M. Morcrette, D. Larcher, L. Laffont, S. Beattie, J.-P. Pérès, D. Talaga, M. Couzi and J.-M. Tarascon, *Adv. Funct. Mater*., 2007, **17**, 1765; (c) M. Holzapfel, H. Buqa, W. Scheifele, P. Novák and F.-M. Petrat, *Chem. Commun*., 2005, **12**, 1566.

7 T. Zhang, J. Gao, H. P. Zhang, L. C. Yang, Y. P. Wu and H. Q. Wu, *Electrochem. Commun*., 2007, **9**, 886.

8 (a) Y.-S. Hu, R. Demir-Cakan, M.-M. Titirici, J.-O. Müller, R. Schlögl, M. Antonietti and J. Maier, *Angew. Chem. Int. Ed*., 2008, **47**, 1645; (b) L. W. Su, Z. Zhou and M. M. Ren, *Chem. Commun*., 2010, **46**, 2590.

9 (a) J. Lee, M. C. Orilall, S. C. Warren, M. Kamperman, F. J. DiSalvo and U. Wiesner, *Nature Mater*., 2008, **7**, 222; (b) F. Jiao, J. Bao, A. Hill and P. Bruce, *Angew. Chem. Int. Ed*., 2008, **47**, 9711; (c) Y. Zhou, Y. Kim, C. Jo, J. Lee, C. W. Lee and S. Yoon, *Chem. Commun*., 2011, **47**, 4944; (d) H. Kim and J. Cho, *Nano Lett*., 2008, **8**, 3688.

10 Q. J. He, J. L. Shi, X. Z. Cui, C. Y. Wei, L. X. Zhang, W. Wu, W. B. Bu, H. R. Chen and H. X. Wu, *Chem. Commun*., 2011, **47**, 7947.

11 (a) L. Skuja, *J. Non-Cryst. Solids*, 1998, **239**, 16; (b) V. S. Kortov, A. F. Zatsepin, V. A. Pustovarov, A. A. Chudinov and D. Yu. Biryukov, *Radiat. Meas*., 2007, **42**, 891; (c) H. Nishikawa, E. Watanabe, D. Ito and Y. Ohki, *Phys. Rev. Lett*., 1994, **72**, 2101.

12 (a) F. Chen, Z. Shi and M. Liu, *Chem. Commun*., 2000, **21**, 2095; (b) N. Baccile, C. V. Teixeira, H. Amenitsch, F. Villain, M Lindén and F. Babonneau, *Chem. Mater*., 2008, **20**, 1161; (c) Q. He, X. Cui, F. Cui, L. Guo and J. Shi, *Microporous Mesoporous Mater*., 2009, **117**, 609.

13 (a) M. N. Obrovac and L. Christensen, *Electrochem. Solid-State Lett*., 2004, **7**, A93; (b) S. H. Ng, J. Wang, K. Konstantinov, D. Wexler, S. Y. Chew, Z. P. Guo and H. K. Liu, *J. Power Sources*, 2007, **174**, 823; (c) I. Sandu, P. Moreau, D. Guyomard, T. Brousse, L. Roué, *Solid State Ionics*, 2007, **178**, 1297.

14 (a) E. Yoo, J. Kim, E. Hosono, H.-S. Zhou, T. Kudo and I. Honma, *Nano Lett*., 2008, **8**, 2277; (b) B. J. Landi, M. J. Ganter, C. D. Cress, R. A. DiLeo and R. P. Raffaelle, *Energy Environ. Sci*., 2009, **2**, 638; (f) M. Pumera, *Energy Environ. Sci*., 2011, **4**, 668.

15 (a) K. Chang and W. Chen, *ACS Nano*, 2011, **5**, 4720; (b) X. Wang, Q. Xiang, B. Liu, L. Wang, T. Luo, D. Chen and G. Shen, *Sci. Rep*., 2013, **3**, 2007; (c) X. Huang, J. Chen, Z. Lu, H. Yu, Q. Yan and H. H. Hng, *Sci. Rep*., 2013, **3**, 2317.

16 S. Yang, H. Song and X. Chen, *Electrochem. Commun*., 2006, **8**, 137.